Available online at www.sciencedirect.com

SCIENCE DIRECT

Surface & Coatings Technology 194 (2005) 119–127

SURFACE & COATINGS TECHNOLOGY

www.elsevier.com/locate/surfcoat

Investigation of nanocrystal-$(Ti_{1-x}Al_x)N_y$/amorphous-Si_3N_4 nanolaminate films

Bao-Shun Yau[a], Jow-Lay Huang[a,*], Horng-Hwa Lu[b], Pavol Sajgalik[c]

[a] Department of Materials Science and Engineering, National Cheng-Kung University, Tainan 701, Taiwan, ROC
[b] Department of Mechanical Engineering, National Chin-Yi Institute of Technology, Taichung 411, Taiwan, ROC
[c] Institute of Inorganic Chemistry, Slovak Academy of Sciences, Dúbravská cesta 9, SK-842 36 Bratislava, Slovakia

Received 5 February 2004; accepted in revised form 7 May 2004
Available online 6 July 2004

Abstract

Nanocrystal-$(Ti_{1-x}Al_x)N_y$/amorphous-Si_3N_4 nanolaminate films were deposited periodically via reactive magnetron sputtering technique. The effects of the thickness of multilayer period on the microstructure and mechanical properties were investigated by X-ray diffraction, scanning and transmission electron microscopies, nanoindentation and scratching adhesion testing. Results indicate that the nanolaminate structure is uniform and good flatness interfaces under different multilayer periods. The nanolaminate films exhibited a maximum hardness when the multilayer structure had a period of $\lambda = 25$ nm and were harder than monolayer $(Ti_{1-x}Al_x)N_y$ or Si_3N_4 films of the same thickness. The critical scratching load of the nanolaminates was higher than that of monolayer specimens with the same thickness. The mechanisms of fracture and toughening of nanolaminate films are also discussed.
© 2004 Published by Elsevier B.V.

Keywords: Reactive sputtering; Multilayer; Nanostructure; Nanoindentation; Scratch test

1. Introduction

Microstructural design is one of the best ways to enhance the mechanical properties of film materials. A new superhard coating with nanocrystalline/amorphous (nc/a) structure was shown to have considerable hardness enhancement as compared with monolithic materials [1,2]. Previous results indicated that the strengthening mechanism of nanocrystalline/amorphous composite films was dislocation pinning. Dislocations formed in the crystallites under a higher applied stress could not freely move through the amorphous matrix, and therefore the strength of the materials was enhanced [1,2].

In recent years, ceramic superhard compositionally modulated multilayer films have been actively investigated [3–5]. Results have shown that multilayer films can show improved performance over monolayer films and combine the attractive properties of different materials in a single protective layer. The introduction of a number of interfaces parallel to the substrate surface can act to deflect cracks and provide barriers to dislocation motion [6]. For layer only a few nanometers thick, dislocation generation mechanism cannot operate. These effects will lead to a considerable reduction in total dislocation mobility and thus a hardening and strengthening of the materials [6].

Cutting tool materials with (Ti,Al)N coating have been shown to be superior to other conventional binary coatings and could be used at significantly higher cutting speed [7] since the oxidation resistance was improved [8–10].

Silicon nitride films are useful for structural applications due to their attractive properties of hardness and chemical inertness. It was reported that an amorphous matrix, such as Si_3N_4, could provide a higher stability against oxidation than that of crystalline metallic nitride [1]. Therefore, nanolaminate materials consisting of nanocrystal-$(Ti_{1-x}Al_x)N_y$ and amorphous-Si_3N_4 [designated as nc-$(Ti_{1-x}Al_x)N_y$ and a-Si_3N_4] can be seen as future novel cutting tool coating materials.

In the present study, nc-$(Ti_{1-x}Al_x)N_y$/a-Si_3N_4 nanolaminate films were synthesized via a reactive magnetron sputtering technique. The effects of the thickness of multi-

* Corresponding author. Tel.: +886-6-234-8188; fax: +886-6-276-3586.
E-mail address: JLH888@mail.ncku.edu.tw (J.-L. Huang).

0257-8972/$ - see front matter © 2004 Published by Elsevier B.V.
doi:10.1016/j.surfcoat.2004.05.009

layer period (λ) on the microstructure and mechanical properties were investigated.

2. Experimental procedure

2.1. Synthesis

Nanocrystal-$(Ti_{1-x}Al_x)N_y$/amorphous-Si_3N_4 nanolaminate films were deposited from Ti–Al alloy (50/50 at.% 99.99% purity, 7.62 cm in diameter, 0.64 cm in thickness, Plamaterial, USA) and Si targets (99.999% purity, 7.62 cm in diameter, 0.64 cm in thickness, Target Materials, USA) by alternating covering shutters. The thickness ratio of the nc-$(Ti_{1-x}Al_x)N_y$ layer to the a-Si_3N_4 layer is 1:1, and the multilayer period λ is the sum of both layers. The films were coated on silicon wafers for X-ray diffraction analysis because the (200) peak of TiAlN severely overlapped with a Fe peak. For other properties analysis, the film was deposited on high-speed steel (HSS, SKH51). The HSS substrates were annealed at 860 °C, quenched from 1220 °C and then tempered at 550 °C. A Rockwell C hardness of 64 HRC (800 HV) was obtained after heat treatment. Substrates were machined into blocks of 15 × 15 × 5 mm and polished with diamond particles with grain sizes down to 1 μm, degreased and ultrasonically cleaned in acetone and ethyl alcohol and subsequently dried in flowing nitrogen gas before deposition. In order to enhance the adhesion and to reduce the effects of the substrate, TiAl films (0.3 μm) were first deposited as an interlayer.

The deposition system (Fig. 1) is a rectangular vacuum chamber with two separated Ti–Al alloy and Si targets. The target-to-substrate distance was 5 cm. The pressure was measured using a hot cathode ion gauge and a thermal couple vacuum gauge. Two separate mass flow controllers (MKS MFC-1179) were used to monitor the gas flow rate of argon and nitrogen. A cryo-pump coupled with a rotary pump was used to achieve an ultimate pressure of 2.7×10^{-4} Pa before introducing gas mixtures of argon and nitrogen. The films were deposited without substrate bias voltage. The targets were firstly pre-sputtered at 0.8 Pa for 10 min in Ar for cleaning. The substrate temperature was maintained at 300 °C. The deposition conditions were presented in Table 1. Deposited samples were cooled down to room temperature in vacuum before venting the system.

Table 1
Deposition conditions for $(Ti_{1-x}Al_x)N_y/Si_3N_4$ nanolaminate films

Parameters	
Flow rate of Ar	50 ml/min
Flow rate of N_2	10 ml/min
DC power to Ti–Al target	200 W
RF power to Si target	200 W
Deposition pressure	0.8 Pa
Temperature of substrate	300 °C
Rotating speed substrate	12 rpm
Negative bias voltage	0V
Total film thickness	1 μm

2.2. Characterization

An X-ray photoelectron spectroscopy (XPS, VG Scientific 210, West Sussex, UK) was used to investigate the composition of the films. The phases, textures and crystallite size of the nanolaminate films were determined by X-ray diffraction using Cu K_α radiation (XRD, Rigaku D/MAX2500, Tokyo, Japan). The elemental depth profiling of nanolaminate films was examined by Auger electron spectroscopy (AES, Fison microlab 310-D, West Sussex, UK). The primary electron beam used was 10 keV with a current of 400 nA. The Auger electron spectra were acquired using a spherical sector analyzer (SSA) with an energy resolution of 0.5%. A backscattered electron (BSE)

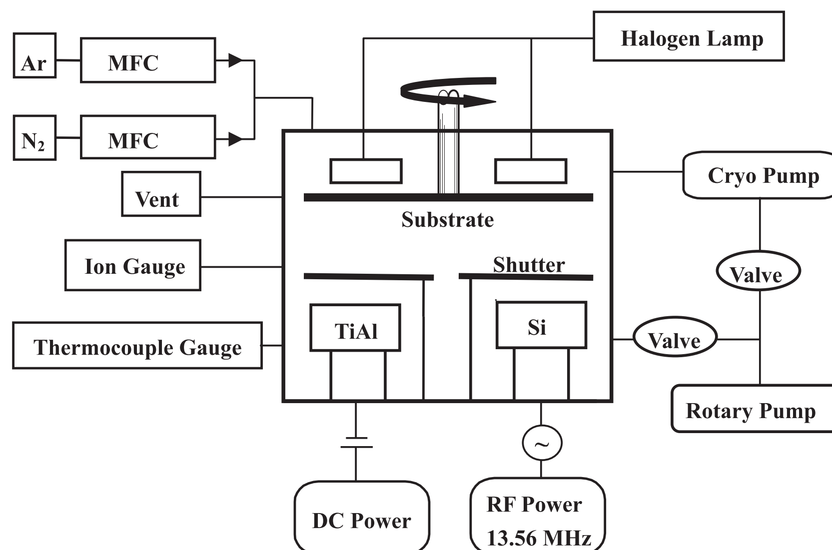

Fig. 1. Schematic diagram of sputtering system for nanolaminate films deposition.

field emission scanning electron microscope (Fe-SEM, XL-40FEG, Philips, Eindhoven, Holland) was used to identify the constituent structure. The microstructure was investigated by field emission gun transmission electron microscopy (FEG-TEM, Hitachi Model HF-2000, Tokyo, Japan).

The hardness of films was evaluated using a Hysitron nanoindentation apparatus interfaced with a Digital Nanoscope II AFM (Digital Instruments, NanoScope, California, USA). An indenter with a three-faced pyramidal diamond tip was used. The indentation depth was less than 10% of the film thickness to reduce the effects of the substrate.

The adhesive strength of each coating was measured by a scratching adhesion tester (RomulusIII Universal Tester, Quad, Japan). A stylus with radius of 300 μm was drawn over the sample surface for 1 cm under a continuously increasing normal force of 1 N/s until the film became detached. The test table was fixed while a stylus was drawn over the sample surface. The normal force causing detachment was defined as the critical scratching load. The morphology of the scratched channel was observed by SEM.

3. Results and discussions

3.1. Composition and microstructure

The compositions of monolayer $(Ti_{1-x}Al_x)N_y$ and monolayer Si_3N_4 films are shown in Table 2. Results indicated that both films were understoichiometric. The ultimate pressure attained in the present work is $\sim 2.7 \times 10^{-4}$ Pa. There is possibility for the films to be contaminated with oxygen [11]. The peak fitted XPS Ti2p spectra for the monolayer $(Ti_{1-x}Al_x)N_y$ and that of Si2p spectra for the monolayer Si_3N_4 films deposited at $\lambda = 100$ nm are shown in Fig. 2. The Al2p region for $(Ti_{1-x}Al_x)N_y$ is not shown due to the very small chemical shift between Al_2O_3 and TiAlN. The graphic showed two envelopes corresponding to the spin-orbit splitting $2p_{1/2}$ (right) and $2p_{3/2}$ (left), with a band shift of about 5.6–5.7 eV, in good agreement with literature [12]. In Fig. 2(a), peak 1 of the $(Ti_{1-x}Al_x)N_y$ sample is attributed to Ti–O bonding. Peak 2 is attributed to Ti–O–N intermediate-phase bonding and peak 3 to T–N bonding [13–15]. From Fig. 2(b), peak 1 of the a-Si_3N_4 sample is attributable to Si–O bonding and peak 2 is attributable to Si–N bonding [16]. The formation of oxide and oxynitride could be the reason that both the nc-$(Ti_{1-x}Al_x)N_y$ and a-Si_3N_4 films were non-stoichiometric.

Table 2
Composition of monolayer $(Ti_{1-x}Al_x)N_y$ and monolayer Si_3N_4 films as determined by XPS analysis

	[Ti] (at.%)	[Al] (at.%)	[N] (at.%)	[Si] (at.%)
nc-$(Ti_{1-x}Al_x)N_y$	31.8	32.2	36	
a-Si_3N_4			55.8	44.2

X-ray diffraction patterns of $(Ti_{1-x}Al_x)N_y/Si_3N_4$ nanolaminate films with different λ are shown in Fig. 3. The (111), (200), (220) and (311) peaks were found and attributed to $(Ti_{1-x}Al_x)N_y$ [17,18]. There was no evidence of crystalline peaks corresponding to the Si_3N_4 film. It suggested therefore that the Si_3N_4 film formed as amorphous structure.

To investigate the composition distribution of films, AES elemental depth profiling was conducted. Fig. 4 reveals the results of films with $\lambda = 100$ nm. The signal of Ti, Al, N and Si were presented periodically, which suggested that the Ti–Al–N and Si–N layers formed alternatively. The combination of N and Ti was due to severe overlap of the Auger peaks. The period of profiles of Ti, Al, N and Si signals was quite similar. It indicated that the composition of each $(Ti_{1-x}Al_x)N_y$ or Si_3N_4 layer was quite repeatable.

A typical backscattered electron SEM micrograph illustrating the cross section of nanolaminate films with $\lambda = 100$ nm is shown in Fig. 5. The difference in backscattered signal contrast between the layers was due to different films having different atomic number [19]. The TEM micrograph of cross section and selective area diffraction (SAD) pattern for $(Ti_{1-x}Al_x)N_y/Si_3N_4$ nanolaminate films with $\lambda = 20$ nm are shown in Fig. 6. The dark area image of the nanolaminate structure was assigned to $(Ti_{1-x}Al_x)N_y$ due to its higher average atomic number [20]. The layers indicated periodic compositional modulation. A diffraction ring with (111), (200) and (220) of fcc $(Ti_{1-x}Al_x)N_y$ structure was in agreement with the XRD results shown in Fig. 3. The diffuse pattern in Fig. 6(b) was assigned to the amorphous Si_3N_4 phase.

The low-angle X-ray diffraction can provide information about interface state of short-period multilayer films [21,22]. Kayushina et al. [22] investigated self-assembled lysozyme/polyion multilayer, and the X-ray reflectivity method was applied for monitoring multilayer film formation. Results indicated that multilayer film appeared X-ray reflectivity curves with Kiessig fringes, which resulted from interference of X-ray reflected from good flatness interface between layers. The X-ray reflectivity patterns with well-defined Kiessig fringes indicate good flatness interface of multilayer film. Fig. 7 shows low-angle X-ray diffraction patterns of c-$(Ti_{1-x}Al_x)N_y$ /a-Si_3N_4 nanolaminate films with different λ. Results indicated X-ray reflectivity curves with Kiessig fringes, which resulted from interference of X-ray reflected from the interface between layers. It is thus suggested that the interface of c-$(Ti_{1-x}Al_x)N_y$/a-Si_3N_4 nanolaminate films were good flatness. It was reported previously that providing flatness interfaces could inhibit dislocation motion and enhance the strength of materials [6].

The calculation of finite crystallite size by XRD analysis should consider the effects of random strain on films [23]. In the present study, however, high-order reflection peaks of the deposited films were absent (for example, 100, 200, 300 for h00 or 110, 220, 330 for hh0 and so on). The crystallite size of films was calculated by the Scherrer formula [23]. The integral width of (200) Bragg reflection with strong intensity was used. Fig. 8 shows the crystallite

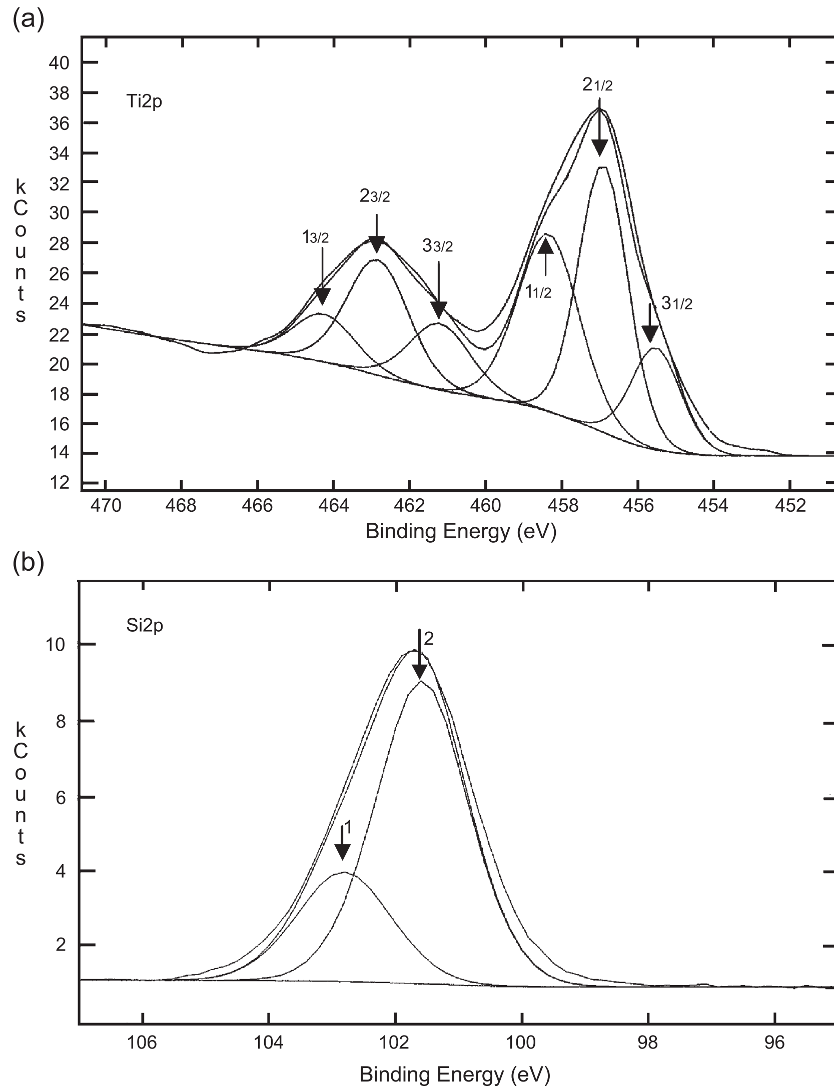

Fig. 2. (a) XPS Ti2p spectra for the monolayer $(Ti_{1-x}Al_x)N_y$ and (b) Si2p spectra for the monolayer Si_3N_4 films deposited at $\lambda = 100$ nm.

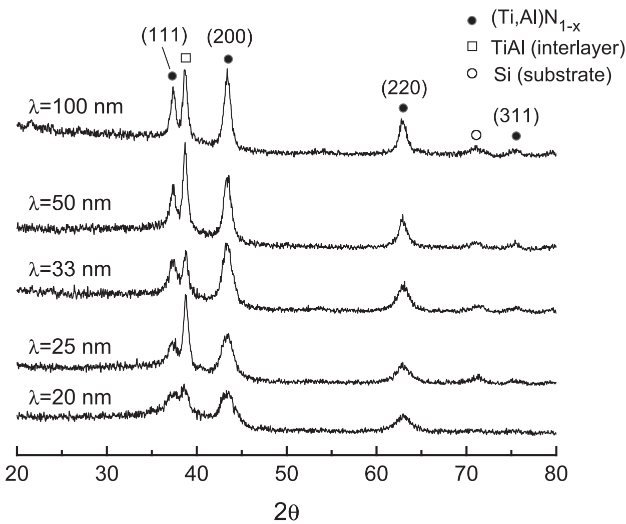

Fig. 3. X-ray diffraction patterns of $(Ti_{1-x}Al_x)N_y/Si_3N_4$ films with different λ.

size of c-$(Ti_{1-x}Al_x)N_y$/a-Si_3N_4 nanolaminate films with different λ. The calculated results indicate that the crystallite size invariably decreased with decreasing λ. A minimum crystallite size of 2.5 nm was obtained as $\lambda = 20$ nm. Decreasing λ implied decreasing time to deposit each layer and therefore reduced time for crystal growth. Similar results were observed by Hausmann and Gordon [24] which investigated the nanolaminates in the context of the crystal nucleation and growth model. Results indicated that the growth of crystallites after the nucleation event had occurred could be prevented with nanolaminate structures. This strategy requires that the second material being deposited does not nucleate and grow crystallites. When a second material is deposited on the top of the growing crystallites, crystallite growth will cease if the second material does not crystallize epitaxially on the top of the preexisting crystallites. By producing a nanolaminate structure, in which the materials formed alternating layers, the size of the crystallites could be effectively capped. In the

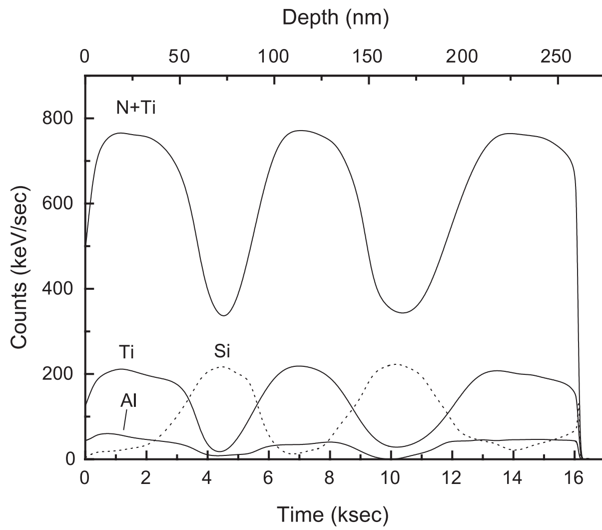

Fig. 4. The AES elemental depth profiling of films deposited at $\lambda = 100$ nm.

present study, amorphous-Si_3N_4 does not have an epitaxial relation to crystal-$(Ti_{1-x}Al_x)N_y$. Therefore, amorphous-Si_3N_4 deposited on the top of crystal-$(Ti_{1-x}Al_x)N_y$ layer can inhibit crystallite growth and nanocrystalline $(Ti_{1-x}Al_x)N_y$ layers are obtained.

Fig. 9 shows AFM images of nc-$(Ti_{1-x}Al_x)N_y$/a-Si_3N_4 nanolaminate films with different λ. Results indicated that the surface morphology of conical features became finer with decreasing λ. Results also indicated that the roughness decreased with the decrease of λ, probably due to the corresponding decrease of the grain size [25,26].

3.2. Mechanical properties

3.2.1. Nanoindentation analysis

Fig. 10 shows that the hardness, plotted as a function of λ for nc-$(Ti_{1-x}Al_x)N_y$/a-Si_3N_4 nanolaminate films, were

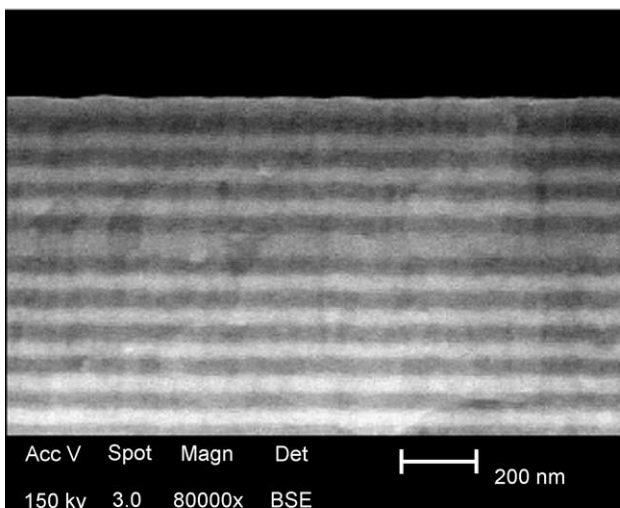

Fig. 5. Typical backscattered electron SEM micrograph illustrating the cross section of nanolaminate films with $\lambda = 100$ nm.

(a)

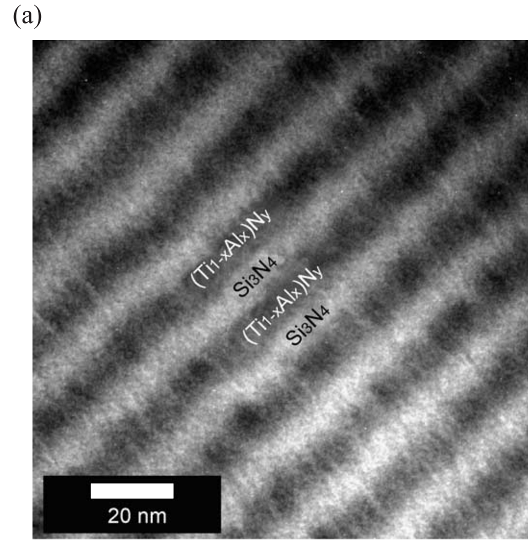

(b)

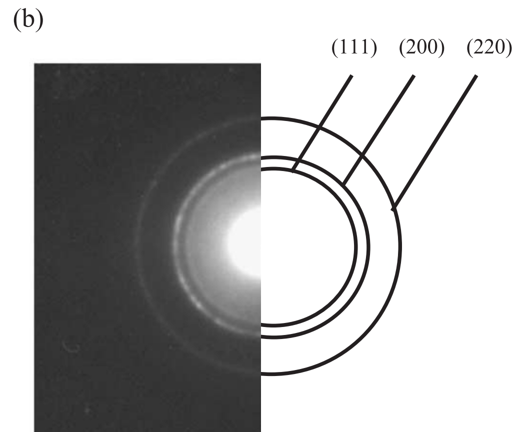

Fig. 6. The TEM micrograph of cross section (a) and selective area diffraction pattern (b) for $(Ti_{1-x}Al_x)N_y/Si_3N_4$ nanolaminate films with $\lambda = 20$ nm.

substantially larger than the rule-of-mixtures value of ~ 16.5 GPa. The hardness of nc-$(Ti_{1-x}Al_x)N_y$ and a-Si_3N_4 films deposited at the same gas pressure is marked

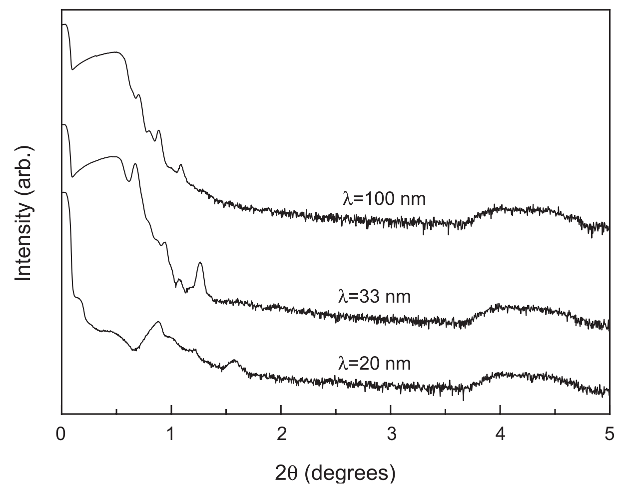

Fig. 7. Low-angle X-ray diffraction patterns of $(Ti_{1-x}Al_x)N_y/Si_3N_4$ nanolaminate films with different λ.

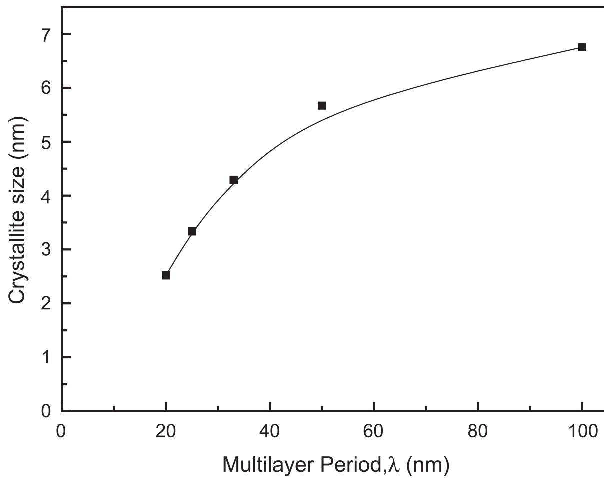

Fig. 8. Crystallite size of nc-$(Ti_{1-x}Al_x)N_y$/a-Si_3N_4 nanolaminate films with different λ.

on the same figure. Results indicated that a maximum hardness of 35 GPa was obtained as $\lambda = 25$ nm. This value exhibited a substantial increase of hardness by 84% and 133% as compared to the monolayer nc-$(Ti_{1-x}Al_x)N_y$ (19 GPa) [27] and monolayer a-Si_3N_4 films (15 GPa) [28], respectively.

In general, improvements in performance for multilayer films are found as λ is decreased, but there are some dramatic changes at very low λ, which have been attributed to the supermodulus effect [3] (Fig. 10b). No such dramatic increases in hardness were observed in the present study and it is not possible for supermodulus effect. Koehler [29] proposed a model for increasing the strength of materials by inhibiting dislocation mobility through the formation of a compositionally modulated structure. If there is a sufficiently large difference in the dislocation line energy of alternating layers, dislocations in one layer will not be able to penetrate the interfaces and dislocation pile-ups will occur. Furthermore, if the layer thicknesses are small enough, dislocation generation mechanisms such as Frank–Read sources cannot operate inside a given layer. These effects give rise to considerable reduction in total dislocation mobility and thus harden the material. For nc-$(Ti_{1-x}Al_x)N_y$/a-Si_3N_4 nanolaminate films, the presence of layers interfered with dislocation motion over a range of λ (20–100 nm) could harden the material. However, the increase in hardness is relatively small. Similar results of the relatively small enhancement of hardness with decreasing λ were reported by Bull and Jones [6].

Mirkarimi et al. [20] investigated the enhancement of hardness in single-crystal $TiN/V_{0.6}Nb_{0.4}N$ superlattices as a

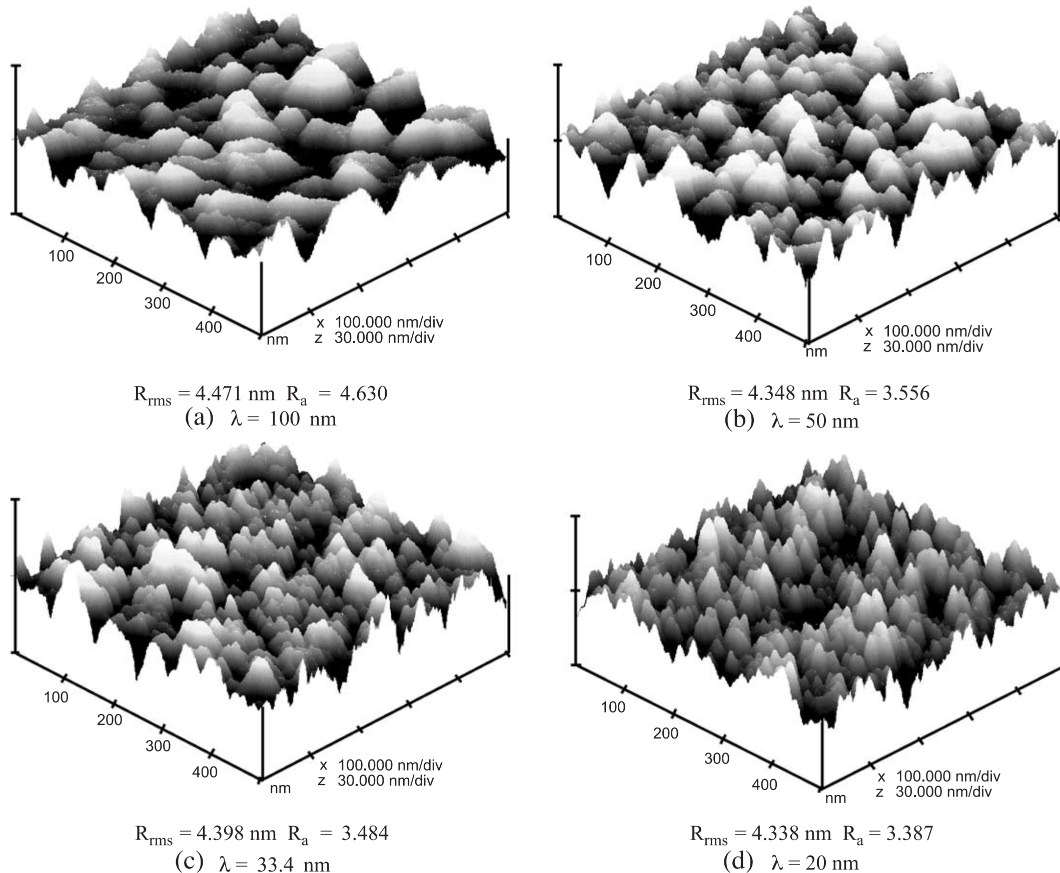

Fig. 9. AFM images showing the morphology and roughness of nc-$(Ti_{1-x}Al_x)N_y$/a-Si_3N_4 nanolaminate films with different λ. (a) $\lambda = 100$ nm, (b) $\lambda = 50$ nm, (c) $\lambda = 33.4$ nm and (d) $\lambda = 20$ nm.

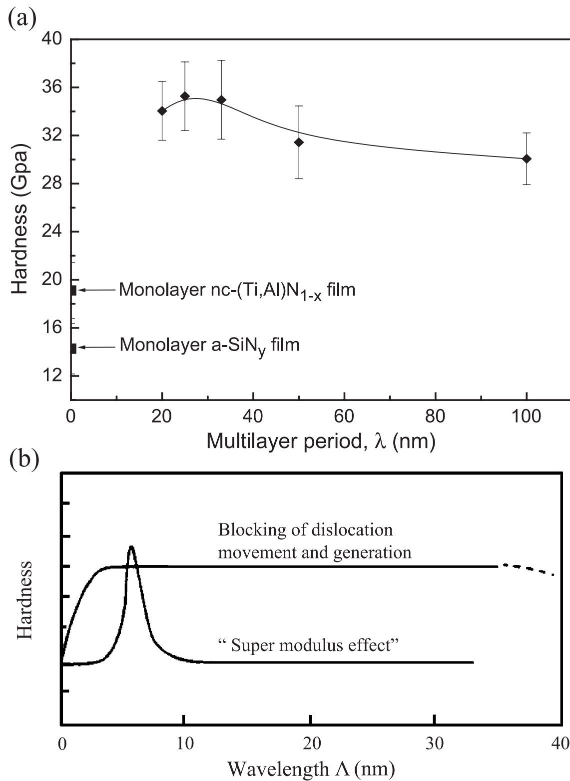

Fig. 10. (a) The hardness of nc-$(Ti_{1-x}Al_x)N_y$/a-Si_3N_4 nanolaminate films with different λ. (b) Schematic diagram showing two possible contributions to the hardness behavior shown in (a).

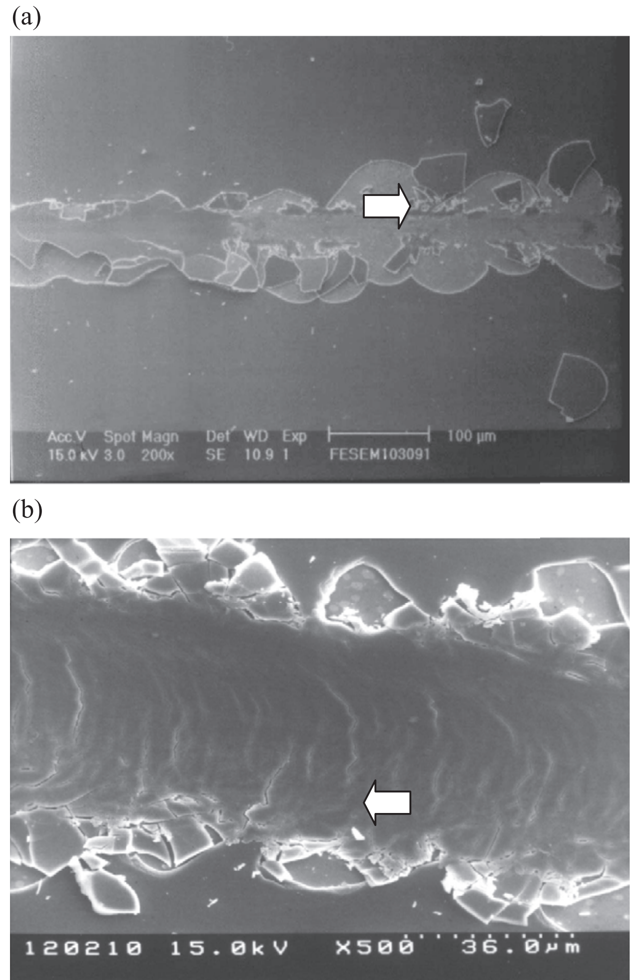

Fig. 11. Typical SEM micrographs showing a scratched channel of monolayer nc-$(Ti_{1-x}Al_x)N_y$ film (a) and nc-$(Ti_{1-x}Al_x)N_y$/a-Si_3N_4 nanolaminate films (b) coated on high-speed steel.

function of superlattice period and reported that the maximum hardness should occur at the point where the greatest density of interfaces is achieved without interdiffusion becoming too great. Shin and Dove [30] investigated the hardness versus individual layer thickness for W/W–N and Hf/Hf–N multilayer films and reported that the major factor for the increase of hardness of multilayer films was due to the small grain-size effect by artificially making each individual thin layer. Similar results of the enhancement of hardness with decreasing λ were reported for TiN/NbN superlattice coating [31] and Si_3N_4/TiN ceramic nanomultilayer films [32].

3.2.2. Adhesion analysis

Typical SEM micrographs of a scratched channel of monolayer nc-$(Ti_{1-x}Al_x)N_y$ film and nc-$(Ti_{1-x}Al_x)N_y$/a-Si_3N_4 nanolaminate film ($\lambda=25$ nm) are shown in Fig. 11. The monolayer nc-$(Ti_{1-x}Al_x)N_y$ film exhibited typical spalling fracture phenomenon. The spalling failure occurred at the critical scratching load as a result of the compressive shear stress generated ahead of the moving stylus (Fig. 11a) [33]. For the nc-$(Ti_{1-x}Al_x)N_y$/a-Si_3N_4 nanolaminate film (Fig. 11b), there were numerous irregular microcracks on the contact site. In this failure mode [33], the scratch groove showed that the propagation of microcracks was caused by the high compressive stress developed in front of indenter and tensile stress behind the indenter. These stresses create delamination at the interface between layers of the film, not delamination at the interface between film and substrate. The lateral cracks emanating from the indenter edge were activated leading to the film's removal by chipping. Similar fracture phenomenon mechanisms in nanoscale-layered hard thin films observation were investigated by Karimi et al. [34].

The critical scratching load for nc-$(Ti_{1-x}Al_x)N_y$/a-Si_3N_4 nanolaminate films with different λ is shown in Table 3. Results indicated that the critical scratching load had no obvious change with increasing λ. A maximum critical

Table 3
Critical scratching load of nc-$(Ti_{1-x}Al_x)N_y$/a-Si_3N_4 nanolaminate films with different λ

Multilayer period λ (nm)	20	25	33	50	100
Critical scratching load (N)	42.6	43.8	42.8	43.6	45.8

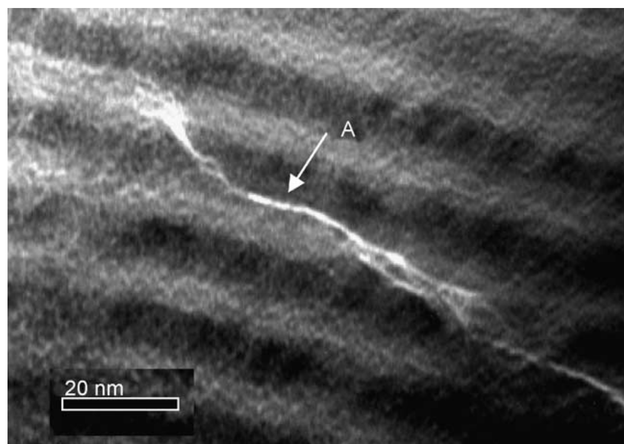

Fig. 12. The cross-section TEM micrograph showed the propagation of nanocracks in nc-$(Ti_{1-x}Al_x)N_y$/a-Si_3N_4 nanolaminate films with $\lambda = 20$ nm.

scratching load of 45 N for nc-$(Ti_{1-x}Al_x)N_y$/a-Si_3N_4 nanolaminate films was obtained. This was a substantial increase by 165% as compared to the monolayer nc-$(Ti_{1-x}Al_x)N_y$ film (17 N). Bull and Jones [6] investigated the adhesion properties of multilayer coatings and reported that the cracks could be deflected by the internal interfaces, which resulted in energy dissipation in the layer material without coating failure. This led to apparent increase in coating toughness and adhesion.

The cross-section TEM micrograph illustrating the propagation of nanocracks in the nanolaminate films with $\lambda = 20$ nm is shown in Fig. 12. Result indicated that the nanocracks could deflect by the internal interface and propagated in the interface between the layers (arrow A). The observation suggested that the toughening effect of nc-$(Ti_{1-x}Al_x)N_y$/a-Si_3N_4 nanolaminate films was attributed to the crack deflection by interface between the layers.

4. Conclusions

Nanocrystal-$(Ti_{1-x}Al_x)N_y$/amorphous-Si_3N_4 nanolaminate films were successfully synthesized via a reactive magnetron sputtering technique. Nanolaminate structure was uniform and good flatness interfaces under different multilayer periods. The a-Si_3N_4 layer inhibited growth of nc-$(Ti_{1-x}Al_x)N_y$ and thus decreased the crystalline size. A minimum crystallite size of 2.5 nm was obtained as $\lambda = 20$ nm.

A maximum hardness of 35 GPa was obtained as $\lambda = 25$ nm, which was better than that of monolayer films with same thickness. The presence of layers interfered with dislocation motion could harden the material. However, the increase in hardness is relatively small.

The mechanism of fracture was transferred from spalling mode to tensile cracking fracture mode as the film with a nanolaminate structure. The critical scratching load of nanolaminate had no obvious change with increasing λ. A maximum critical scratching load of 45 N of nc-$(Ti_{1-x}Al_x)N_y$/a-Si_3N_4 nanolaminate films was obtained, which was better than that of monolayer specimens with same thickness due to the toughness increasing. The toughening mechanism of nc-$(Ti_{1-x}Al_x)N_y$/a-Si_3N_4 nanolaminate films was attributed to the crack deflection by interface between the layers.

Acknowledgements

The authors would like to thank the National Science Council of the Taiwan, ROC for its financial support under the contract no. NSC 91-2216-E006-057.

References

[1] S. Veprek, S. Reiprich, L. Shizhi, Appl. Phys. Lett. 66 (1995) 2640.
[2] S. Veprek, S. Reiprich, Thin Solid Films 268 (1995) 64.
[3] J.-E. Sundgen, J. Birch, G. Hakansson, L. Hultman, U. Helmersson, Thin Solid Films 193–194 (1990) 818.
[4] H. Holleck, H. Schulz, Thin Solid Films 153 (1987) 11.
[5] U. Helmersson, S. Todorova, S.A. Barnett, J.-E. Sundgen, J. Appl. Phys. 62 (1987) 481.
[6] S.J. Bull, A.M. Jones, Surf. Coat. Technol. 78 (1996) 173.
[7] T. Leyendecker, O. Lemmer, S. Esser, J. Edderink, Surf. Coat. Technol. 48 (1991) 175.
[8] J.L. Huang, B.Y. Shew, J. Am. Ceram. Soc. 82 (1999) 696.
[9] W.-D. Münz, J. Vac. Sci. Technol., A, Vac. Surf. Films 4 (1986) 2717.
[10] D. McIntyre, J.E. Greene, G. Håkansson, J.-E. Sundgen, W.-D. Münz, J. Appl. Phys. 67 (1990) 1542.
[11] K.S. Robinson, P.M.A. Sherwood, Surf. Interface Anal. 6 (1984) 261.
[12] J. Lausmaa, Elecon. Spectrosc. Relat. Phenom. 81 (1996) 343.
[13] M.A. Baker, S.J. Greaves, E. Wendler, V. Fox, Thin Solid Films 377–378 (2000) 473.
[14] F.-H. Lu, H.-Y. Chen, Thin Solid Films 355–356 (1999) 374.
[15] R.J. Rodríguez, J.A. García, A. Medrano, M. Rico, R. Sánchez, R. Martínez, C. Labrugère, M. Lahaye, A. Guette, Vacuum 67 (2002) 559.
[16] G.M. Ingo, N. Zacchetti, J. Vac. Sci. Technol., A, Vac. Surf. Films 7 (1989) 3048.
[17] G. Hakasson, J.E. Sundgren, Thin Solid Films 153 (1987) 55.
[18] B.Y. Shew, J.L. Huang, Surf. Coat. Technol. 71 (1995) 30.
[19] J.I. Goldstein, H. Yakowitz, Practical Scanning Electron Microscopy: Electron and Ion Microprobe Analysis, Plenum Press, New York, 1975.
[20] P.B. Mirkarimi, L. Hultman, S.A. Barnett, Appl. Phys. Lett. 57 (1990) 2654.
[21] W.-H. Soe, R. Yamamoto, Mater. Chem. Phys. 50 (1997) 176.
[22] R. Kayushina, Yu. Lvov, N. Stepina, V. Belyaev, Yu. Khurgin, Thin Solid Films 284–285 (1996) 246.
[23] H.P. Klug, L.E. Alexander, X-ray Diffraction Procedures, Wiley, New York, 1974.
[24] D.M. Hausmann, R.G. Gordon, J. Cryst. Growth 249 (2003) 251.
[25] B.K. Tay, X. Shi, H.S. Yang, H.S. Tan, D. Chua, S.Y. Teo, Surf. Coat. Technol. 111 (1999) 229.
[26] J.J. Kim, D.H. Jung, M.S. Kim, S.H. Kim, D.Y. Yoon, Thin Solid Films 409 (2002) 28.
[27] B.S. Yau, J.L. Huang, D.F. Lii, P. Sajgalik, Surf. Coat. Technol. 177–178 (2004) 209.

[28] B.S. Yau, J.L. Huang, Surf. Coat. Technol. 176 (2004) 290.
[29] J.S. Koehler, Phys. Rev., B 2 (1970) 547.
[30] K.K. Shin, D.B. Dove, Appl. Phys. Lett. 61 (1992) 654.
[31] X. Chu, S.A. Barnett, M.S. Wong, W.D. Sproul, Surf. Coat. Technol. 57 (1993) 13.
[32] J.H. Xu, M.Y. Gu, G.Y. Li, Y.P. Jin, Trans. Nonferr. Met. Soc. China 9 (1999) 764.
[33] P.J. Burnett, D.S. Rickerby, Thin Solid Films 154 (1987) 403.
[34] A. Karimi, Y. Wang, T. Cselle, M. Morstein, Thin Solid Films 420–421 (2002) 275.